Experiments in Fluids (2019) 60:123
https://doi.org/10.1007/s00348-019-2772-8

RESEARCH ARTICLE

Shortwave infrared imaging setup to study entrained air bubble dynamics in a MEMS-based piezo-acoustic inkjet printhead

Arjan Fraters[1] · Tim Segers[1] · Marc van den Berg[2] · Hans Reinten[2] · Herman Wijshoff[2,3] · Detlef Lohse[1] · Michel Versluis[1]

Received: 5 December 2018 / Revised: 24 April 2019 / Accepted: 20 June 2019 / Published online: 11 July 2019

Abstract

Piezo-acoustic inkjet printing is the method of choice for high-frequency and high-precision drop-on-demand inkjet printing. However, the method has its limitations due to bubble entrainment into the nozzle, leading to jetting instabilities. In this work, entrained air bubbles were visualized in a micrometer scale ink channel inside a silicon chip of a MEMS-based piezo-acoustic inkjet printhead. As silicon is semi-transparent for optical imaging with shortwave infrared (SWIR) light, a highly sensitive SWIR imaging setup was developed which exploited the optical window of silicon at 1550 nm. Infrared recordings of entrained bubbles are presented, showing rich phenomena of acoustically driven bubble dynamics inside the printhead.

Graphic abstract

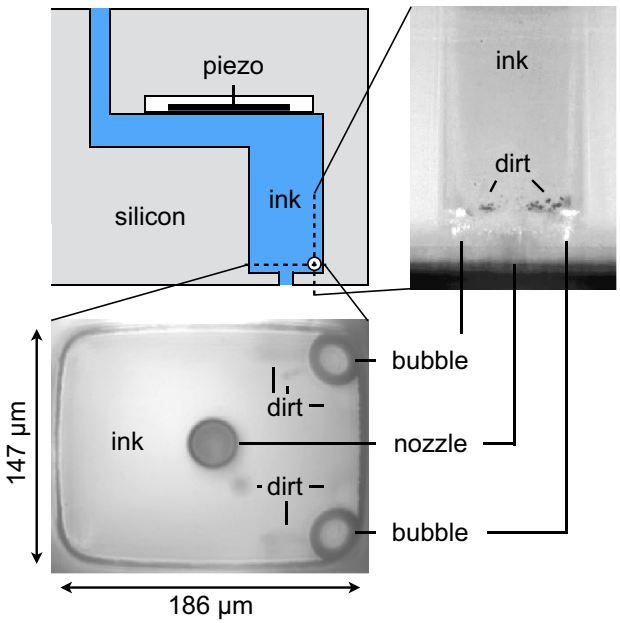

1 Introduction

Piezo-acoustic inkjet printing is a versatile drop deposition technique and a key technology in modern industrial digital printing. With this technique, a piezo-acoustic printhead can jet single droplets on demand out of the nozzles, by driving the ink out of the nozzle thanks to the deformation

Electronic supplementary material The online version of this article (https://doi.org/10.1007/s00348-019-2772-8) contains supplementary material, which is available to authorized users.

✉ Arjan Fraters
abfraters@gmail.com

Extended author information available on the last page of the article

of a piezoelectric element and the resulting pressure field. The technique provides accurate contactless deposition of ink droplets onto a wide variety of substrates, and it can handle inks within a large range of viscosities, surface tensions, and (chemical) compositions. Typically, droplets can be produced with a volume of 1–32 pL, the jetting frequency ranges between 10 and 100 kHz, and the final droplet velocity ranges from 5 to 10 m/s (Wijshoff 2010; Hoath 2015). These capabilities make it an attractive technique both for classical applications such as document printing, packaging, and graphic arts, as well as for novel applications such as 3D printing (Derby 2015), electronic components (Majee et al. 2016, 2017; Eshkalak et al. 2017; Vilardell et al. 2013; Moya et al. 2017; Eggenhuisen et al. 2015; Hashmi et al. 2015; Shimoda et al. 2003; Jiang et al. 2017), and (artificial) biological material (Simaite et al. 2016; Hewes et al. 2017; Nakamura et al. 2005; Villar et al. 2013).

Competition with offset printing in the large volume printing market and the rapid developments in the previously mentioned novel printing applications lead to a constant pursuit for higher productivity, higher printing quality, higher reliability and robustness, and lower costs. Therefore droplet size and production tolerances and costs must decrease, while at the same time jetting frequency, droplet velocity, and resolution (nozzles per inch) must increase. These demands led to a shift towards the use of the Micro-Electro-Mechanical Systems (MEMS) technology (Menzel et al. 2004; Kim et al. 2009; van der Bos et al. 2011; Kim et al. 2014) that is most well known for its widespread use in the silicon-based semiconductor industry for the miniaturization of computer chips and sensors. MEMS technology is replacing classic printheads with ink channels made in, for example graphite, using bulk piezos and a metal nozzle plates (Wijshoff 2010), by printheads with ink channels etched in silicon, having thin film piezos (van der Bos et al. 2011). The main advantages of MEMS technology in silicon are a lower fabrication cost, a higher fabrication precision, a higher nozzle density, and shorter ink channels, allowing more efficient and controlled high DOD frequency jetting.

Figure 1 shows a schematic drawing of an ink channel in a MEMS printhead developed at Océ Technologies. MEMS printheads have shorter ink channels than classic printheads, i.e. of the order of 1 mm instead of 10 mm, and therefore the acoustic operating principle is also different, i.e. Helmholtz resonance (von Helmholtz 1895) instead of the traveling wave principle (Wijshoff 2010).

An essential part of reliable printhead operation is the minimization of air bubble entrainment, which can occur at the nozzle, typically at a timescale of the order of 1 µs, and with an initial bubble radius of the order of 1 µm. As described in de Jong et al. (2006a, b); Jeurissen et al. (2008, 2009); Lee et al. (2009); Jeurissen et al. (2011); van der Bos et al. (2011), entrained air bubbles grow in the acoustic field

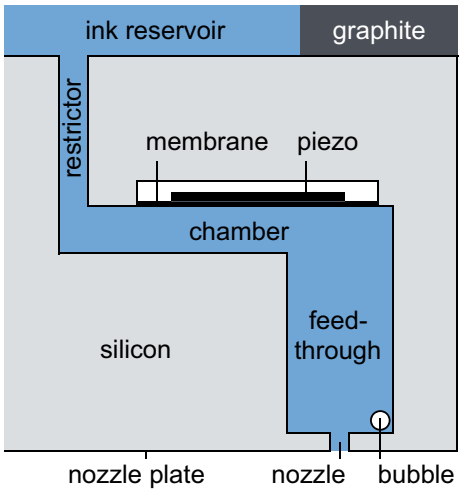

Fig. 1 Layout of MEMS-based printhead ink channel with an entrained air bubble. The nozzle has a length and diameter of 30 µm

inside the ink channel due to rectified diffusion (Eller and Flynn 1965; Crum 1984; Leighton 1994; Brennen 1995; Brenner et al. 2002), move to a wall due to acoustic radiation forces, and distort or even halt drop formation because their compressibility affects the acoustic pressure at the nozzle. Thus air entrainment has a detrimental effect on the printing quality and reliability. Therefore the ultimate goal is to fully understand the bubble entrainment mechanisms and subsequent bubble dynamics, so that printheads can be designed with a minimal chance of entrainment or at least a minimal influence of entrained bubbles on the droplet formation.

In classic printheads both dust particles and an ink layer on the nozzle plate have been shown to induce air bubble entrainment (de Jong et al. 2006a). Air entrainment through these mechanisms can be prevented by applying an anti-wetting coating to the nozzle plate, as this prevents transport of ink and dirt to jetting nozzles. Entrained bubbles were visualized in the classic printhead by replacement of the metal nozzle plate by a glass chip with ink channel-extensions terminated by nozzles. A major drawback of this method was its invasiveness, especially because of the hourglass shape of the ink channels and conical shape of the nozzles due to limitations of the powder-blasting method that was utilized to form the channels and nozzles in glass. The optically accessible glass channels were imaged using a high-speed camera at a framerate of 40 kfps and at a spatial resolution of 4 µm/pixel (de Jong et al. 2006b). The bubble growth and translation could be studied from shortly after entrainment to its fully developed state. However, the imaging system was not capable of recording the entrainment process itself due to the short timescales of this process.

MEMS printheads can also suffer from bubbles that disrupt the drop formation process (Kim et al. 2009; van der

Bos et al. 2011). As silicon is semi-transparent (50–60%) to infrared light with wavelengths between 1.1 and 6.0 µm, it is possible to look into silicon devices using infrared imaging (Chung et al. 2003; Han et al. 2004; Liu et al. 2005). In our prior work (van der Bos et al. 2011), this was done in MEMS printhead at a shortwave infrared (SWIR) wavelength of 1.2 µm. Entrained bubbles were observed in the feedthrough of a MEMS printhead that experienced jetting failure. The steady-state oscillations and the dissolution of fully grown bubbles were studied, and it was shown that the size of a single entrained bubble could be calculated based on only a measurement of the channel acoustics, measured through the piezo electronics. However, the entrainment process itself, and the subsequent bubble growth and translation from just after entrainment to a fully grown bubble, could not be imaged because of the limited (infrared) optical accessibility of the feedthrough through the nozzle plate, the lack of a side view into the nozzle and feedthrough, and the limited image quality, including resolution, sensitivity, and frame rate of the imaging system. So despite these previous efforts, a full understanding of the physical mechanisms involved in the bubble entrainment process and bubble dynamics is still lacking.

To overcome this shortcoming, in this work more details of the entrained air bubble dynamics in a MEMS printhead have been revealed using a newly developed, highly sensitive SWIR imaging setup, and a more recent MEMS printhead design of which the feedthroughs and nozzles are more accessible to SWIR imaging. With the new setup single bubbles were imaged in much more detail, as well as multiple bubbles and their mutual interactions. The observed phenomena include bubble growth and translation, merging of bubbles, steady-state dynamics of fully grown bubbles, long-term bubble stability, and acoustic streaming.

2 Experimental system

2.1 Printhead and ink

For this study an experimental MEMS printhead from Océ Technologies was selected and externally modified without making intrusive modifications to the functional acoustic part of the printhead. The most important requirement for this MEMS printhead was a good optical accessibility to SWIR imaging of the feedthroughs and nozzles (see Fig. 1) through both the bottom and side of the MEMS chip. Because of the large difference in refractive index n between the silicon ($n = 3.5$), the ink ($n = 1.5$) and the air ($n = 1.0$), the critical angles of total internal reflection for the silicon–air and the silicon–ink interfaces are only 16.6° and 25.4°, respectively (van der Bos et al. 2011). Therefore the internal and external walls should ideally be smooth and oriented either perpendicular or parallel to the optical path. Deviations from the ideal orientation deteriorate the image quality and quickly result in total reflection. Therefore a MEMS chip design was chosen with all features either parallel or perpendicular to the nozzle plate, i.e., one that has no funnel between the feedthrough and the nozzle, as we had in van der Bos et al. (2011). Furthermore, the feedthrough in the selected chip design has a rectangularly shaped cross-section with rounded corners instead of a circular one, as in van der Bos et al. (2011). The optical path for the side view into the chip was created through a few special modifications. First, a layer of silicon was polished away from the side of the selected MEMS chip to minimize the optical path length in the silicon. Second, the modified chip was glued onto the printhead such that the bottom half of the polished side of the chip remained optically accessible. Lastly, an anti-wetting coating, consisting of self-assembled monolayers of (Tridecafluoro-1,1,2,2-tetrahydrooctyl)trichlorosilane (FOTS, abcr GmbH, CAS 78560-45-9), was applied to the polished side of the chip to prevent the formation of an ink layer that may distort the imaging process. The front of the nozzle plate, where the nozzle exits are located, did not suffer from the formation of an optically distorting ink layer, and therefore did not require an anti-wetting coating to achieve optical access. The nozzles were cylindrical and had a length and diameter of 30 µm. As model ink a non-colored version of the CrystalPoint^{TM} technology (Océ Technologies B.V.) was used, which is a hot melt ink that is jetted at 130 °C. At this temperature the ink's viscosity, density, and surface tension are 10 mPa s, 1080 kg/m^3, and 28 mN/m, respectively.

The printhead was actuated at a drop-on-demand (DOD) frequency of 20 kHz using a trapezoidal pulse with a rise- and fall time of 1.5 µs, and with a high time of 2 µs, optimized for an ink channel Helmholtz resonance frequency of 143 kHz. This piezo driving pulse was produced by an arbitrary waveform generator (Wavetek 195) and amplified by a broadband power amplifier (Krohn-Hite 7602M) to an actuation amplitude of 40 V, corresponding to a droplet velocity of 7 m/s. The ink channel acoustics could be monitored through a custom-made electronic device that measures the piezo current due to the piezo deformation by pressure fluctuations in the ink channel in between the actuation pulses. The piezo signals were recorded at maximum at 50 Hz, i.e., once every 400 actuation pulses, by an oscilloscope (Tektronix TDS5034B) at a sampling rate of 50 MHz. The recorded signals were stored onto a PC using a custom-made Labview program for offline processing.

2.2 SWIR imaging system

The shortwave infrared (SWIR) imaging system, shown in Fig. 2, consisted of a reflected light microscope (Olympus,

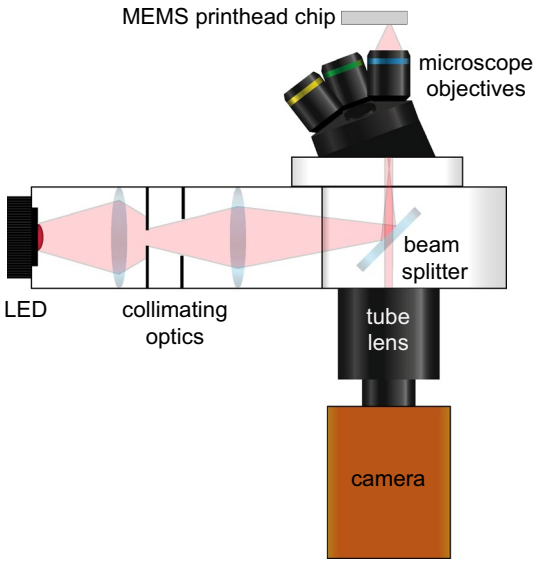

Fig. 2 Reflected light shortwave infrared imaging setup for imaging entrained air bubbles in the ink channels of a MEMS-based printhead

BX-URA2) with SWIR-compatible components, i.e., a 50:50 beamsplitter (Thorlabs, BSW29R, wavelength range: 600–1700 nm), a 50× microscope objective (Olympus, LCPLN50XIR, N.A. 0.65, working distance 4.5 mm) and a tube lens (Olympus, U-TLU IR). Illumination was provided by an infrared Light-Emitting Diode (LED, Epitex, L1550-66-60-130, 1550 nm, 60 mW). A light source wavelength of 1550 nm, which is within the SWIR camera sensor range of 900–1700 nm and is widely used in optical communication systems, was chosen over 1200 nm as it resulted in higher quality images, see Fig. 3. The LED was used both in continuous mode by directly connecting it to a power supply

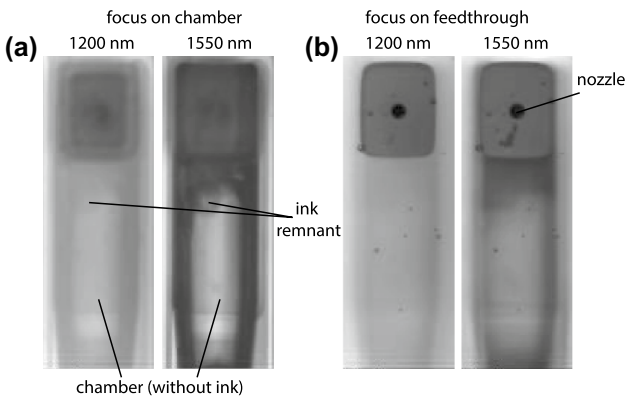

Fig. 3 Comparison between 1200 nm and 1550 nm illumination. The images of the exact same ink channel are clearly of higher quality for 1550 nm illumination. **a** Shows images of the ink channel with the optical focus on the chamber whereas in **b** the optical focus was positioned at the feedthrough. Note the ink remnants in the otherwise empty ink chamber that can only be clearly appreciated using 1550 nm illumination

unit (Delta, max. 60 V and 0.6 A), and in stroboscopic mode by connecting it to a custom-made electronic driving circuit. The stroboscopic driving circuit was designed to limit motion blur while maintaining sufficient light intensity. It delivered a large current to the LED during 500 ns pulses by discharging two capacitors (Philips, 0.68 µF, 100 V, 0.68/10/100 MKT 344 H0) via a fast switching power MOSFET with an ultra-low on-resistance (International Rectifier, HexFET Power MOSFET, IRF540Z, 29.5 mΩ, cont.: 34 A, pulsed: 140 A). Due to the short illumination time and limited brightness of the light source, every image required 1800 light flashes over a camera exposure time of 90 ms. A SWIR camera (Raptor Photonics, Ninox 640, SCD InGaAs PIN-Photodiode sensor, 640×512 pixels, 15 µm pixel pitch) was attached to the microscope to record images at a resolution of 0.305 µm/pixel. The recorded images were stored onto a PC using a custom-made Labview program. Triggering of the printhead actuation, the stroboscopic illumination, and the camera recording was performed by a digital delay/pulse generator (Berkeley Nucleonics Corp, BNC 575) with nanosecond precision.

2.3 SWIR camera sensor selection

The camera of the SWIR imaging system was selected based on the results of a sensitivity and image quality characterization test for three different camera sensors. The three sensors were selected primarily based on their sensitivity (quantum efficiency, dynamic range, and dark current), the pixel pitch, and the number of pixels. The sensitivity is important in view of the short illumination times required to freeze the motion of an oscillating bubble of micrometer size. A small pixel pitch is desirable because it requires less magnification and resulting light loss. A large number of pixels is desirable to get high resolution images. All three sensors were Indium Gallium Arsenide (InGaAs) sensors. More information on architectural differences between the sensors was not publicly available. The basic characteristics of the tested camera sensors are summarized in Table 1.

The sensitivity of the sensors was tested using the setup illustrated in Fig. 4a. Note that this characterization setup is different from the imaging setup presented in Sect. 2.2. It had a transmitted light microscope (Olympus, BXFM-F

Table 1 Demo camera sensor characteristics: pixel array size, pixel pitch, and maximum frame rate

	Sensor 1	Sensor 2	Sensor 3
Size (px)	1280 × 1024	640 × 512	640 × 512
Pitch (µm)	12.5	15	20
Rate (fps)	60	90	400

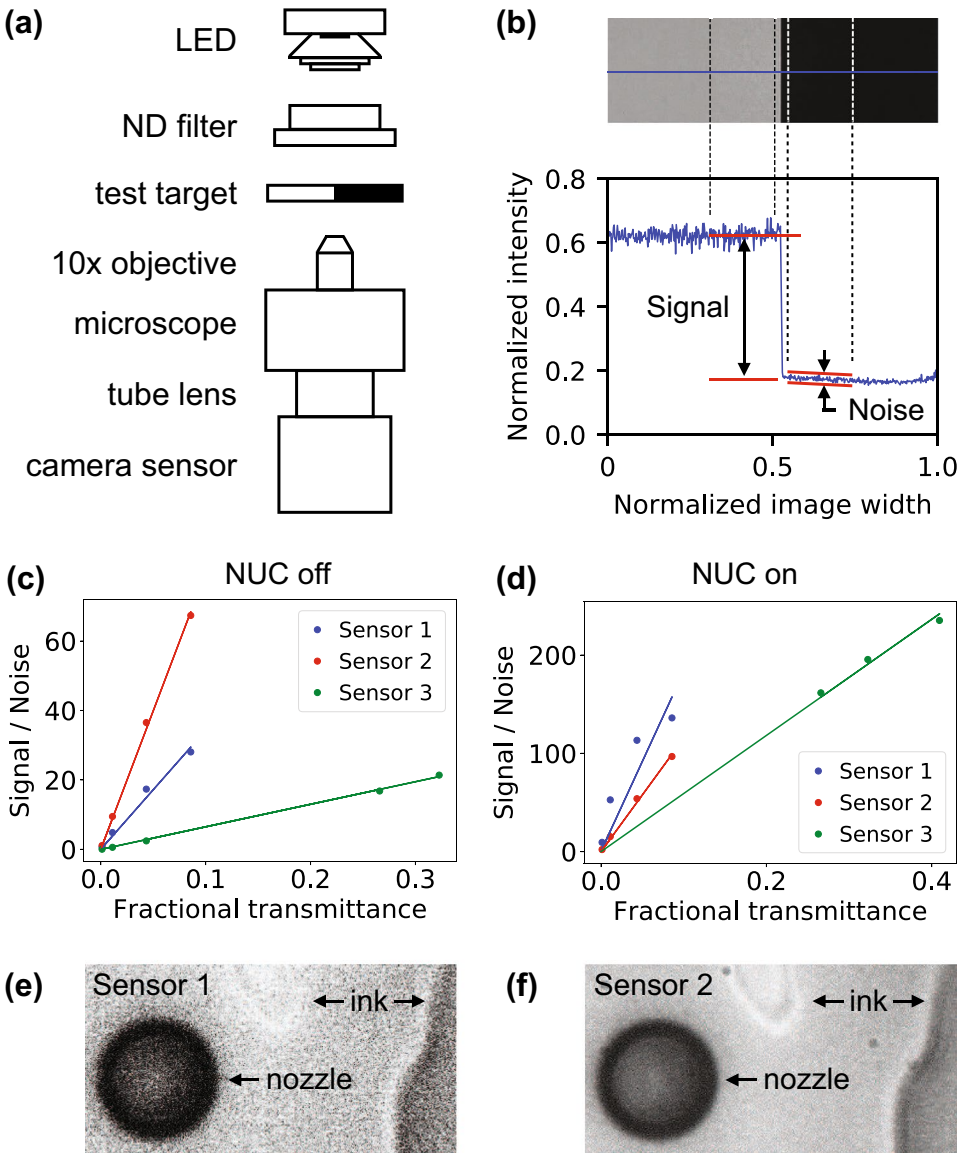

Fig. 4 **a** Camera sensor sensitivity measurement setup. **b** Part of a sensitivity image with below it a plot of the intensity values of the pixels on the blue line. Signal and noise are extracted from the light and dark region in between the dashed lines. **c**, **d** Signal-to-noise ratio at 500 µs exposure time with non-uniformity correction off and on, respectively. **e**, **f** Image quality at low-light condition during stroboscopic imaging of an inkjet nozzle (30 µm diameter) in bottom view using the imaging setup in Fig. 2

+ BXFM-ILHS + U-DP) with a 10× infrared microscope objective (Olympus, LMPLN10XIR, N.A. 0.3, working distance 18 mm) and an infrared tube lens (Olympus, U-TLU IR). The LED, the same as in the other setup, emitted light continuously at full power, and measurements were performed at neutral density (ND) filter fractional transmittance values between 1 (no filter) and 0.001 (Thorlabs, NENIRxxA where x = number between 0 and 9), and at exposure times between 50 µs and 10 ms. A test target (Thorlabs, R3L3S1N, Negative 1951 USAF Test Target, 3”×3”) was placed in the optical path to form an image with a light and dark region, separated by a sharp transition. All recordings were performed in the most sensitive mode of each sensor, usually called the high gain mode. The sensors were tested both with non-uniformity correction (NUC) off and on. The NUC corrects for bad pixels, and for differences between the pixel offset, gain, and dark current, because each pixel has its own A/D converter.

Figure 4b shows part of a typical recording by the sensitivity test setup, and illustrates how the signal and noise were determined from such an image using a script programmed in Python (Python Software Foundation, https://www.python.org/). For both the light section in between the black dashed lines and the dark section in between the white dashed lines the mean pixel value was calculated, and the difference between the two was defined as the signal. The noise was extracted from the dark pixel array section in between the white dashed lines. First the array was flattened by subtracting the baseline, a polyfit plane of order 10 fitted to this array, from it. Then the noise was obtained by calculating the standard deviation of the flattened array.

The measurement results are summarized in Fig. 4c, d. From these results it was concluded that Sensor 3 could not compete with the other two sensors, because it had a much lower signal-to-noise ratio at the same light intensity. The differences between Sensor 1 and Sensor 2 were less evident. As a final test, a bottom view recording was made of an ink channel in the MEMS printhead with stroboscopic illumination using the imaging setup shown in Fig. 2, and using the same number of light flashes per image. Figure 4e, f show the nozzle and thin ink layers on the nozzle plate. The noise level of the image recorded using Sensor 2 was lower than that of the image recorded by Sensor 1. Therefore Sensor 2 was selected for the SWIR imaging setup.

2.4 Image quality and optical accessibility

The SWIR imaging system's image quality and optical access to the feedthroughs and nozzles of the MEMS-based printhead are demonstrated in Fig. 5. In both the image of the bottom view and that of the side view two entrained air bubbles are visible, as well as dirt particles that collected around the bubbles and the nozzle. The bottom view shows an actuated channel with fast streaming around the bubbles and the nozzle due to acoustic streaming. So particles are blurred because of their motion, in contrast to the side view. In the side view, showing a non-actuated channel, the bubbles are not as clearly visible because the feedthrough side wall was not as straight and smooth as the bottom of the feedthrough. In the side view also the nozzle could not be clearly imaged and the meniscus could not be visualized,

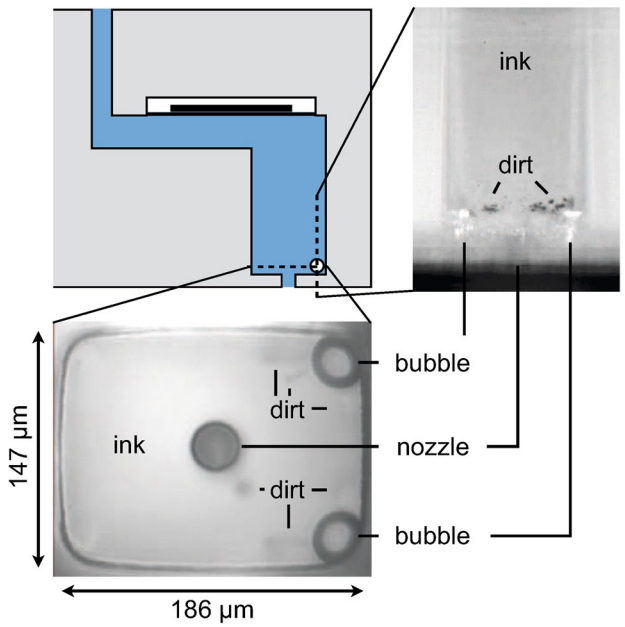

Fig. 5 Typical bottom view and side view of an ink channel in the MEMS printhead imaged by the shortwave infrared imaging setup

which is a result of the combination of a cylindrical nozzle shape with the small critical angles of total internal reflection of the silicon interfaces with ink and air. This underlines the imaging challenges involved. Nevertheless, the image quality of the present setup is dramatically increased with respect to that earlier presented (van der Bos et al. 2011), see Supplementary Fig. S1.

2.5 Experimental settings and image processing

The growth, translation, and interaction of bubbles from just after entrainment to a fully grown state were captured by real-time imaging at a frame rate of 50 or 60 fps, using continuous SWIR illumination. The steady-state dynamics of fully grown bubbles during one drop-on-demand period of 50 µs were captured stroboscopically at a temporal resolution of 0.5 µs. In the stroboscopic recording mode an image and a piezo signal were captured once every 0.4 s, to allow the computer to store the data and change the settings of the pulse delay generator.

The contrast between the bubbles and the background in the recorded images was enhanced with the image processing program ImageJ (http://imagej.nih.gov/ij). In the experiments for which a reference image was available with an ink channel without bubbles and particles, the contrast between the feedthrough wall and the bubble was increased by first subtracting the bubble image from the reference image, and then subtracting the resulting image from the bubble image. Furthermore, the function 'subtract background' in ImageJ was used to filter out the uneven illumination in some parts of the background. Finally, contrast was enhanced by adapting the image histogram.

3 Experimental observations

3.1 Bubble entrainment

A typical recording of bubble entrainment is shown in Fig. 6 and Supplementary Video 1. Initially, multiple bubbles of different sizes, here with diameters between 3 and 8 µm, were entrained and spread along the feedthrough wall at the intersection with the nozzle plate. The maximum frame rate of 90 fps was not high enough to capture the entrainment process and the origin of the observed multiple bubbles. The bubbles remained positioned at their initial location for at least 20 ms, grew by rectified diffusion (Eller and Flynn 1965; Crum 1984; Leighton 1994; Brennen 1995; Brenner et al. 2002), and at a certain moment moved to a corner. These movements are explained by secondary Bjerknes forces (Leighton 1994; Brennen 1995; Brenner et al. 2002; Garbin et al. 2009) attracting bubbles to the wall and into the corner, and by

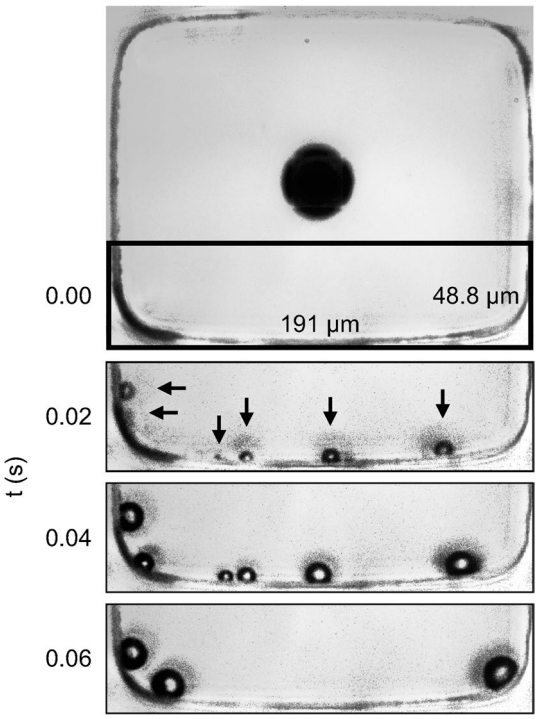

Fig. 6 Real-time 50 fps bottom view recording of bubble entrainment, with t being the time after entrainment. The shadow around the bubbles is caused by motion blur due to oscillation of the bubbles at the microsecond timescale during actuation. See also Supplementary Video 1

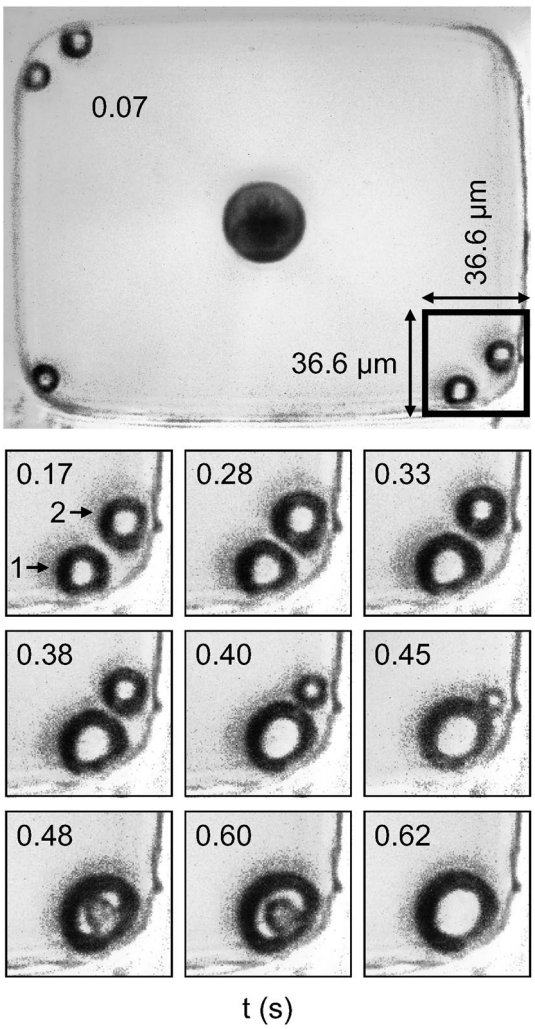

Fig. 7 Real-time 60 fps recording of diffusive interaction between two bubbles in the same corner, with t being time after entrainment. The shadow around the bubbles is caused by motion blur due to the oscillations of the bubbles at the microsecond timescale during actuation. See also Supplementary Video 2

wall roughness holding bubbles temporarily in place along the wall. Multiple bubbles located at a single corner interacted and either quickly merged or coexisted in a semi-stable equilibrium; some bubbles coexisted stably for up to at least several minutes.

The dynamics of the entrained bubbles shown in Fig. 6 and Supplementary Video 1 are representative for the overall behavior of all imaged bubble entrainment events. First, the entrained bubbles disperse along the feedthrough wall at the intersection with the nozzle plate. Second, the bubbles grow through rectified diffusion. During the unsteady growth phase, secondary Bjerknes forces drive the bubbles towards a corner. In the corner, a steady state is reached where the bubbles either merge through coalescence and/or Ostwald ripening or where they stably co-exist. Despite the similar overall dynamics, the details of the individual entrainment cases were observed to be remarkably different. The existence of the various entrained bubble configurations and entrained bubble dynamics reflect the stochastic nature, complexity, and richness of bubble entrainment phenomena in piezo-driven inkjet printheads. In the remaining sections, we present typical examples of the range of bubble configurations observed over many bubble entrainment events.

3.2 Merging of bubbles by Ostwald ripening

In the case that multiple bubbles were present in the same corner, and merged, it was not necessarily due to coalescence. In multiple occasions an Ostwald ripening (Ostwald 1897; Lemlich 1978; Tcholakova et al. 2011; Lee et al. 2015)-type of process was observed, i.e. exchange of gas between bubbles by diffusion of gas through the liquid. An example is shown in Fig. 7 and Supplementary Video 2. Initially, the two bubbles in the bottom-right corner of the channel approached each other and grew due to rectified diffusion. Between $t = 0.28$ s and $t = 0.45$ s bubble 2 shrunk, while bubble 1 grew, i.e., a large portion of the gas from bubble 2 diffused through the surrounding liquid into bubble 1. The gas exchange here was more complicated than

in conventional Ostwald ripening, as not only the Laplace pressure in the bubbles played a role, but the bubbles were also prone to rectified diffusion, a process that is affected by the presence of the wall, bubble (shape) oscillations, surfactants, and acoustic streaming (Gould 1974; Crum 1980; Leong et al. 2011). After $t = 0.45$ s bubble 2 moved behind bubble 1, and between $t = 0.60$ s and $t = 0.62$ s bubble 2 disappeared.

3.3 Steady-state dynamics of fully grown bubbles

Within a few seconds after entrainment, the bubbles reached an equilibrium state in which the number of bubbles, the bubble sizes, and the bubble positions remained constant. This allowed for the use of stroboscopic imaging to study the steady-state bubble dynamics. Figure 8a and Supplementary Video 3 show four of the observed equilibrium bubble configurations: Fig. 8a-a a single bubble, Fig. 8a, b two bubbles of different size, Fig. 8a–c two bubbles of a similar size, and Fig. 8a–d three bubbles of which two were of a similar size. The images in each column show the following five different states of the bubble dynamics: (1) at rest, (2) at the first maximum expansion, (3) first maximum compression, (4) asymmetric bubble collapse towards the wall, and 5. the second maximum expansion. The estimated total volumes of the bubbles at rest in the four cases were 22 pL, 8.9 pL, 4.9 pL, and 2.5 pL, respectively. Figure 8b, c show that in all four cases the presence of bubbles in the ink channel can be acoustically detected. Figure 8b presents the piezo signals of the four cases with bubbles and of one case without bubbles. Figure 8c displays the Fourier transform of these signals over the region between 7.5 and 50 µs, i.e., after the piezo actuation, as indicated by the region with the grey background in Fig. 8b. Thus, the entrainment of a single bubble in a channel with initially no bubbles resulted in an increase of the peak frequency of 43%, from 142 to 203 kHz, while the amplitude of the peak frequency increased by almost a factor of two.

Both, case (a) and (b) in Fig. 8 result in an increase in peak frequency from the Helmholtz resonance mode (143 kHz) to the same value of 200 kHz whereas the total bubble volume in (a) is 2.5 times larger than in (b). This indicates that the acoustic signal measured by the piezo is not just the eigenfrequency f_B of the bubble since $f_B \propto 1/R$ (Leighton 1994). In fact, the frequency response measured by the piezo is that of the coupled ink channel–bubble system. In the linear limit, both the ink channel and the bubble can be described as a mass-spring system (Leighton 1994; Dijksman 1998). Therefore, the eigenfrequency measured by the piezo for an ink channel with an entrained bubble can be modeled as a coupled mass-spring system. Details of this model will be part of a forthcoming paper.

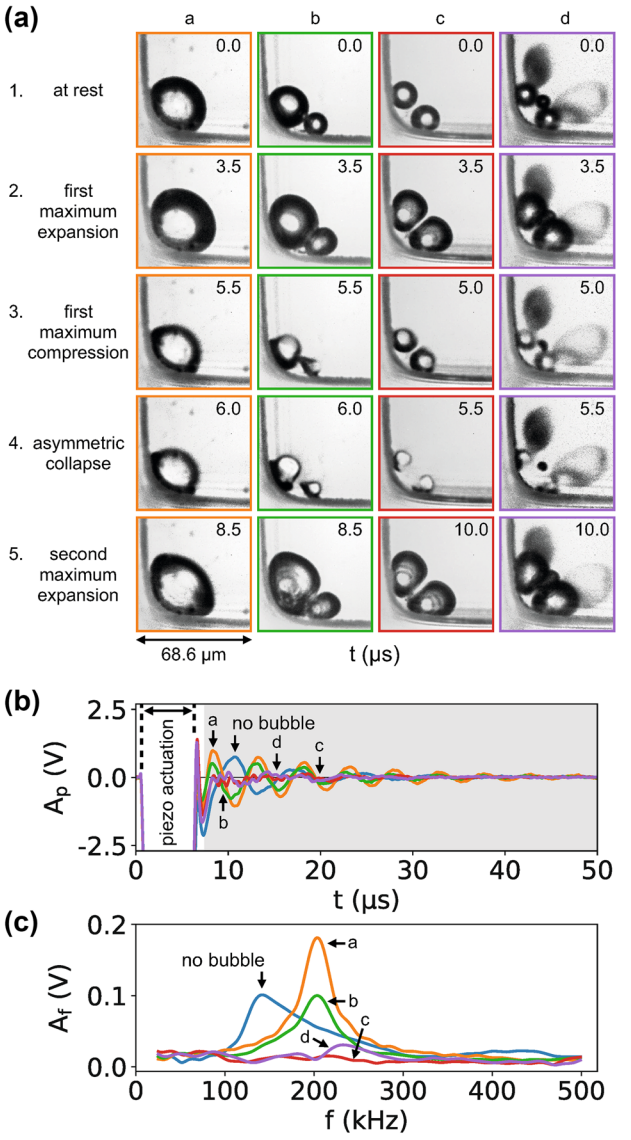

Fig. 8 **a** Stroboscopically recorded images (68.6×68.6 µm) of four different bubble configurations, showing five different stages in their bubble dynamics. t is the time from the start of the actuation pulse in µs. See also Supplementary Video 3. **b** Piezo signals of the four different bubble configurations, and of a reference case with no bubbles in the channel. **c** Fourier transforms of the piezo signals

3.4 Stable coexistence of colliding bubbles

The image sequence in Fig. 9a and Supplementary Video 4 show details of the steady-state volume oscillations of two non-coalescing bubbles of a similar size. During every piezo actuation, the bubbles were acoustically driven into oscillation, and twice the bubbles collided, i.e., their surfaces flattened in the area of close proximity after having approached each other at a finite velocity: the first time for 2.5 µs starting at $t = 2.5$ µs, and the second time for 7.5 µs starting at $t = 8.5$ µs. During these two collisions the bubble surfaces

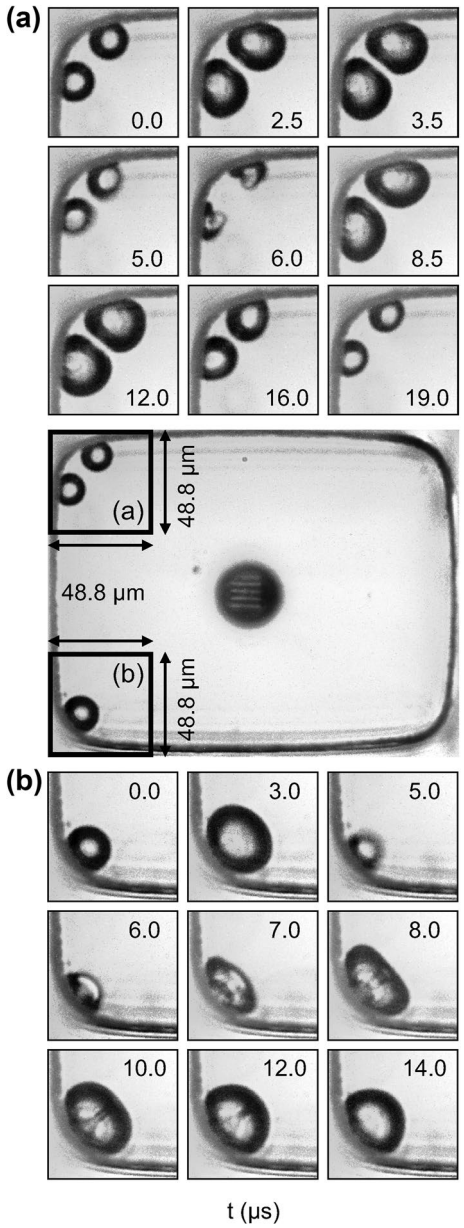

Fig. 9 Two stroboscopically recorded image sequences, with t being the time from the start of the actuation pulse. **a** Two bubbles of a similar size colliding twice during one drop-on-demand period of 50 µs without coalescing. **b** Asymmetric collapse of a single bubble towards the wall, whereby a jet is formed in the bubble directed at the wall, and the bubble gets a toroidal shape. See also Supplementary Video 4

approached each other at an approximate maximum velocity of 2 m/s and 5 m/s, which, with bubble radii of 8 µm and 10 µm, corresponds to Weber numbers of 1.2 and 9.6, respectively. In this high Weber number regime, where the bubble surfaces are flattened during collision, coalescence is delayed by the drainage of the liquid film in between the flat surfaces of the bubbles, especially because of the presence of surface-active components in the ink (Postema et al. 2004). In between the collisions the bubbles asymmetrically collapsed in opposite direction, towards two different sides of the wall at the corner, thereby limiting the contact time between the bubbles and thus also hindering coalescence. This is visible in Fig. 9a at $t = 5.0$ µs to $t = 6.0$ µs, where the distance between the bubble surfaces increased rapidly and the bubble surfaces strongly deformed. During asymmetric collapse of a single bubble in one of the other corners, see Fig. 9b, the deformation was even so large that a jet penetrated the bubble in the direction of the wall, resulting in a toroidal bubble. Asymmetric collapse and microjet formation for bubbles at a wall are well-known phenomena, and are described in detail in Leighton (1994); Brennen (1995); Benjamin and Ellis (1966); Plesset and Chapman (1971); Crum (1979); Lauterborn (1982); Blake et al. (1997); Postema et al. (2005); Vos et al. (2011).

3.5 Acoustic streaming

The flow induced by acoustic streaming (Lighthill 1978; Longuet-Higgins 1998), driven by a phase difference between the volumetric and translational oscillations of the bubble (Marmottant and Hilgenfeldt 2003; Marmottant et al. 2006; Lajoinie et al. 2018), was visible in the experiments due to dirt particles that collected in the streamlines around the bubbles and above the nozzle. This was already briefly discussed in Fig. 5, and is shown in more detail in Fig. 10 and Supplementary Video 5. Here, bubbles were entrained into the channel after 7.5 s of printhead operation, and collected in two corners of which one is shown in the image sequence in Fig. 10a. After having reached an equilibrium state at $t = 8.77$ s, dirt particles collected around the bubbles in streaming patterns as shown at $t = 40.65$ s. The motion blur in the images of the dirt particles is indicative of the high streaming velocity in this experiment. Therefore, the particles could not be tracked to measure flow velocities. However, in future work, the DOD frequency could be substantially lowered to decrease the time-averaged flow velocities which potentially allows for particle tracking velocimetry (PTV) or particle image velocimetry (PIV) such as described by Chung et al. (2003); Han et al. (2004) and Liu et al. (2005). When the actuation was halted, the bubbles dissolved, and in the absence of acoustic streaming the dirt particles were trapped in the viscous surrounding, visible at $t = 40.67$ s and $t = 41.92$ s.

For the nozzle it was observed that during the jetting phase, when no bubbles were entrained, dirt particles were always present near the edge of the nozzle. For example, in Fig. 10 at $t = 7.5$ s a dirt particle is visible in the top right corner of the nozzle. These particles seemed to circle near the nozzle, while their trajectories slightly fluctuated in position around the circumference of the nozzle edge. The presence of dirt particles over a time window of the order of

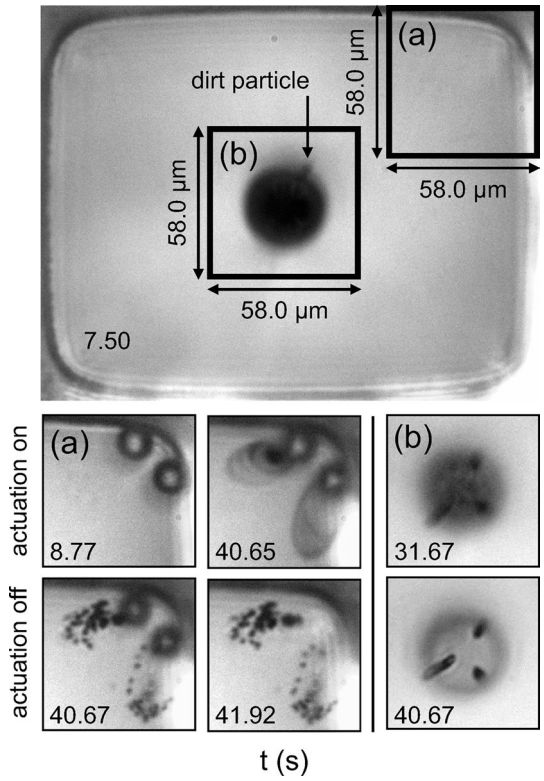

Fig. 10 Real-time 60 fps recording of dirt particles captured in acoustic streaming streamlines, with t being the time after the start of actuation. After $t = 40.65$ s the piezo actuation is turned off. **a** Two coexisting bubbles in the same corner that dissolve once piezo actuation has stopped. **b** Dirt particles that are captured in fixed trajectories above the nozzle. See also Supplementary Video 5

seconds, while the printhead was jetting droplets at 20 kHz, indicates that the dirt particles were trapped. The particles may be trapped in a vortical flow, e.g., as a result of the oscillating meniscus (Mach et al. 2011; Karino and Goldsmith 1977; Zhang et al. 2016). The trapped dirt particles may act as bubble nucleation sites (Brennen 1995).

After bubble entrainment it was observed that the dirt particle trajectories both had periods where they would constantly move around the circumference of the nozzle edge, and periods where they were more fixed at one location above the nozzle edge. Figure 10b shows a time interval where they were more fixed: the three particles visible at $t = 31.67$ s are still at the identical locations at $t = 40.67$ s, which is 9.00 s later, or after approximately 180,000 actuations.

4 Discussion and outlook

The SWIR imaging setup has revealed remarkably rich and complex phenomena of acoustically driven bubble dynamics inside a MEMS-based printhead, in particular the entrainment and interaction of multiple bubbles. However, it was not able to capture the bubble entrainment mechanism because of the limited camera framerate and the optical inaccessibility of the nozzle area. A further limitation of the SWIR setup is the three times higher diffraction limit (1.2 µm) as compared to that of an imaging setup that makes use of visible light. Nevertheless, the imaged bubbles were at least 10 µm in diameter resulting in an error of only approx. 10%.

The main interest of the present SWIR imaging setup is its ability to stroboscopically image in full detail the acoustically driven bubble dynamics at a temporal resolution of 0.5 µs. The fully resolved radial dynamics allows for a direct comparison of the experiments with numerical simulations. The stochastic nature of the bubble entrainment process allows for the combined experimental–numerical study of multiple bubble configurations, i.e., from a single bubble to multiple bubbles in different and/or in the same corner, and for a range of bubble sizes. Modeling the coupling between the ink channel acoustics and the bubble dynamics, which changes the ink channel acoustics, is an interesting acoustics problem from which a gain in fundamental knowledge of ink channel acoustics is expected. Furthermore, it is of interest to further investigate the interaction of two bubbles in the regime where the simultaneous occurrence of Ostwald ripening and rectified diffusion plays an important role. These topics will be part of a future more detailed study.

5 Conclusion

Entrained air bubbles and ink flow in a MEMS-based piezo-acoustic drop-on-demand printhead can be visualized using shortwave infrared (SWIR) imaging because the silicon walls of the ink channels are semi-transparent to infrared light. A highly sensitive SWIR imaging system and a SWIR accessible MEMS-based printhead were developed to study entrained air bubbles in the ink channel. The growth, translation, and interactions of bubbles shortly after entrainment were imaged in real-time at a framerate of 50 fps. The steady-state dynamics of fully grown bubbles were imaged stroboscopically at a temporal resolution of 0.5 µs. In both cases the piezo signal, representing the pressure fluctuations in the ink channel after actuation, was recorded each time an image was captured.

The recordings showed that, shortly after bubble entrainment, initially multiple bubbles of different size were spread along the feedthrough wall at the nozzle plate, and that eventually the bubbles collected at the corners of the feedthrough. The interactions of multiple bubbles in the same corner in some cases led to merging of the bubbles through Ostwald ripening, and in other cases to semi-stably coexisting bubbles. Bubbles coexisting in the same corner

did not merge through coalescence because they collided at high Weber number during the expansion phase and collapsed asymmetrically towards the wall during the compression phase. Acoustic streaming near the nozzle and around entrained bubbles was visible due to the presence of dirt particles that were captured in the streamlines above the nozzle and around the bubbles. These observations demonstrate that with a highly sensitive SWIR imaging system the phenomena of fluid flow and acoustics in silicon devices, such as a MEMS-based piezo-acoustic inkjet printhead, can be studied in detail down to the micrometer lengthscale and at the microsecond timescale.

Acknowledgements We thank the employees from Océ Technologies B.V. for their help with the production of the printhead, in particular Henk Simons, Norbert Lamers, Jos Lemmen, and Henk Stolk. We furthermore thank Bas Benschop from the University of Twente for his help with the production of the electronic systems for the experimental setup. This work is part of the research program "High Tech Systems and Materials" (HTSM) with project number 12802, and part of the Industrial Partnership Program number i43, of the Dutch Technology Foundation (STW) and the Foundation for Fundamental Research on Matter (FOM), which are part of the Netherlands Organisation for Scientific Research (NWO). The research was co-financed by Océ Technologies B.V., University of Twente, and Eindhoven University of Technology.

References

Benjamin T, Ellis A (1966) The collapse of cavitation bubbles and the pressures thereby produced against solid boundaries. Philos Trans R Soc Lond A Math Phys Sci 260(1110):221–240

Blake J, Hooton M, Robinson P, Tong R (1997) Collapsing cavities, toroidal bubbles and jet impact. Philos Trans R Soc A Math Phys Eng Sci 355(1724):537–550

Brennen C (1995) Cavitation and bubble dynamics. Oxford University Press, New York

Brenner M, Hilgenfeldt S, Lohse D (2002) Single-bubble sonoluminescence. Rev Mod Phys 74(2):425–484

Chung J, Grigoropoulos C, Greif R (2003) Infrared thermal velocimetry in MEMS-based fluidic devices. J Microelectromech Syst 12(3):365–372

Crum L (1979) Surface oscillations and jet development in pulsating bubbles. Journal de Physique Colloques 40(C8):285–288

Crum L (1980) Measurements of the growth of air bubbles by rectified diffusion. J Acoust Soc Am 68(1):203–211

Crum L (1984) Rectified diffusion. Ultrasonics 22(5):215–223

de Jong J, de Bruin G, Reinten H, van den Berg M, Wijshoff H, Versluis M, Lohse D (2006a) Air entrapment in piezo-driven inkjet printheads. J Acoust Soc Am 120(3):1257–1265

de Jong J, Jeurissen R, Borel H, van den Berg M, Wijshoff H, Reinten H, Versluis M, Prosperetti A, Lohse D (2006b) Entrapped air bubbles in piezo-driven inkjet printing: their effect on the droplet velocity. Phys Fluids 18(12):121511

Derby B (2015) Additive manufacture of ceramic components by inkjet printing. Engineering 1(1):113–123

Dijksman J (1998) Hydro-acoustics of piezoelectrically driven ink-jet print heads. Flow Turbul Combust 61(1–4):211–237

Eggenhuisen T, Galagan Y, Coenen E, Voorthuijzen W, Slaats M, Kommeren S, Shanmuganam S, Coenen M, Andriessen R, Groen W (2015) Digital fabrication of organic solar cells by inkjet printing using non-halogenated solvents. Solar Energy Mater Solar Cells 134:364–372

Eller A, Flynn H (1965) Rectified diffusion during nonlinear pulsations of cavitation bubbles. J Acoust Soc Am 37(3):493–503

Eshkalak S, Cinnappan A, Jayathilaka W, Khatibzadeh M, Kowsari E, Ramakrishna S (2017) A review on inkjet printing of CNT composites for smart applications. Applied Materials Today 9:372–386

Garbin V, Dollet B, Overvelde M, Cojoc D, Fabrizio ED, van Wijngaarden L, Prosperetti A, de Jong N, Lohse D, Versluis M (2009) History force on coated microbubbles propelled by ultrasound. Phys Fluids 21(9):092003

Gould R (1974) Rectified diffusion in the presence of, and absence of, acoustic streaming. J Acoust Soc Am 56(6):1740–1746

Han G, Bird J, Johan K, Westin A, Cao Z, Breuer K (2004) Infrared diagnostics for measuring fluid and solid motion inside silicon microdevices. Microscale Thermophys Eng 8(2):169–182

Hashmi S, Ozkan M, Halme J, Misic K, Zakeeruddin S, Paltakari J, Grätzel M, Lund P (2015) High performance dye-sensitized solar cells with inkjet printed ionic liquid electrolyte. Nano Energy 17:206–215

von Helmholtz H (1895) On the sensations of tone as a physiological basis for the theory of music. Longmans, Green, and Co, London

Hewes S, Wong A, Searson P (2017) Bioprinting microvessels using and inkjet printer. Bioprinting 7:14–18

Hoath SD (2015) Fundamentals of inkjet printing: the science of inkjet and droplets. Wiley, Oxford

Jeurissen R, de Jong J, Reinten H, van den Berg M, Wijshoff H, Versluis M, Lohse D (2008) Effect of an entrained air bubble on the acoustics of an ink channel. J Acoust Soc Am 123(5):2496–2505

Jeurissen R, van der Bos A, Reinten H, van den Berg M, Wijshoff H, de Jong J, Versluis M, Lohse D (2009) Acoustic measurement of bubble size in an inkjet printhead. J Acoust Soc Am 126(5):2184–2190

Jeurissen R, Wijshoff H, van den Berg M, Reinten H, Lohse D (2011) Regimes of bubble volume oscillations in a pipe. J Acoust Soc Am 130(5):3220–3232

Jiang C, Mu L, Zou J, He Z, Zhong Z, Wang L, Xu M, Wang J, Peng J, Cao Y (2017) Full-color quantum dots active matrix display fabricated by ink-jet printing. Sci China Chem 60(10):1349–1355

Karino T, Goldsmith H (1977) Flow behaviour of blood cells and rigid spheres in an annular vortex. Philos Trans R Soc Lond B Biol Sci 279(967):413–445

Kim BH, Kim TG, Lee TK, Kim S, Shin SJ, Kim SJ, Lee SJ (2009) Effects of trapped air bubbles on frequency responses of the piezo-driven inkjet printheads and visualization of the bubbles using synchrotron X-ray. Sens Actuators A Phys 154(1):132–139

Kim BH, Lee HS, Kim SW, Kang P, Park YS (2014) Hydrodynamic responses of a piezoelectric driven MEMS inkjet print-head. Sens Actuators A Phys 210:131–140

Lajoinie G, Luan Y, Gelderblom E, Dollet B, Mastik F, Dewitte H, Lentacker I, de Jong N, Versluis M (2018) Non-spherical oscillations drive the ultrasound-mediated release from targeted microbubbles. Commun Phys 1:22

Lauterborn W (1982) Cavitation bubble dynamics—new tools for an intricate problem. Appl Sci Res 38(1):165–178

Lee M, Lee E, Lee D, Park B (2015) Stabilization and fabrication of microbubbles: applications for medical purposes and functional materials. Soft Matter 11:2067–2079
Lee S, Kwon D, Choi Y (2009) Dynamics of entrained air bubbles inside a piezodriven inkjet printhead. Appl Phys Lett 95(22):221902
Leighton T (1994) The acoustic bubble. Academic, New York
Lemlich R (1978) Prediction of changes in bubble size distribution due to interbubble gas diffusion in foam. Ind Eng Chem Fund 17(2):89–93
Leong T, Collis J, Manasseh R, Ooi A, Novell A, Bouakaz A, Ahokkumar M, Kentish S (2011) The role of surfactant headgroup, chain length, and cavitation microstreaming on the growth of bubbles by rectified diffusion. J Phys Chem C 115(49):24310–24316
Lighthill J (1978) Acoustic streaming. J Sound Vib 61(3):391–418
Liu D, Garimella S, Wereley S (2005) Infrared micro-particle image velocimetry in silicon-based microdevices. Exp Fluids 38(3):385–392
Longuet-Higgins M (1998) Viscous streaming from an oscillating spherical bubble. Proc R Soc A Math Phys Eng Sci 454(1970):725–742
Mach A, Kim J, Arshi A, Hur S, Carlo DD (2011) Automated cellular sample preparation using a centrifuge-on-a-chip. Lab Chip 11(17):2827–2834
Majee S, Song M, Zhang SL, Zhang ZB (2016) Scalable inkjet printing of shear-exfoliated graphene transparent conductive films. Carbon 102:51–57
Majee S, Liu C, Wu B, Zhang SL, Zhang ZB (2017) Ink-jet printed highly conductive pristine graphene patterns achieved with water-based ink and aqueous doping processing. Carbon 114:77–83
Marmottant P, Hilgenfeldt S (2003) Controlled vesicle deformation and lysis by single oscillating bubbles. Nature 423:153–156
Marmottant P, Versluis M, de Jong N, Hilgenfeldt S, Lohse D (2006) High-speed imaging of an ultrasound-driven bubble in contact with a wall: "Narcissus" effect and resolved acoustic streaming. Exp Fluids 41(2):147–153
Menzel C, Bibl A, Hoisington P (2004) MEMS solutions for precision micro-fluidic dispensing application. Technical Report, Fujifilm Dimatix Inc
Moya A, Gabriel G, Villa R, del Campo FJ (2017) Inkjet-printed electrochemical sensors. Curr Opin Electrochem 3(1):29–39
Nakamura M, Kobayashi A, Takagi F, Watanabe A, Hiruma Y, Ohuchi K, Iwasaki Y, Horie M, Morita I, Takatani S (2005) Biocompatible inkjet printing technique for designed seeding of individual living cells. Tissue Eng 11(11–12):1658–1666
Ostwald W (1897) Studien über die bildung und umwandlung fester körper. Zeitschrift für Physikalische Chemie 22:289–330
Plesset M, Chapman R (1971) Collapse of an initially spherical vapour cavity in the neighbourhood of a solid boundary. J Fluid Mech 47(2):283–290
Postema M, Marmottant P, Lancée C, Hilgenfeldt S, de Jong N (2004) Ultrasound-induced microbubble coalescence. Ultrasound Med Biol 30(10):1337–1344
Postema M, van Wamel A, ten Cate F, de Jong N (2005) High-speed photography during ultrasound illustrates potential therapeutic applications of microbubbles. Med Phys 32(12):3707–3711
Shimoda T, Morii K, Seki S, Kiguchi H (2003) Inkjet printing of light-emitting polymer displays. Inkjet Print Funct Mater 28(11):821–827
Simaite A, Mesnilgrente F, Tondu B, Souères P, Bergaud C (2016) Towards inkjet printable conducting polymer artifical muscles. Sens Actuators B Chem 229:425–433
Tcholakova S, Mitrinova Z, Golemanov K, Denkov N, Vethamuthu M, Ananthapadmanabhan K (2011) Control of Ostwald ripening by using surfactants with high surface modulus. Langmuir 27(24):14807–14819
van der Bos A, Segers T, Jeurissen R, van den Berg M, Reinten H, Wijshoff H, Versluis M, Lohse D (2011) Infrared imaging and acoustic sizing of a bubble inside a micro-electro-mechanical system piezo ink channel. J Appl Phys 110(3):034503
Vilardell M, Granados X, Ricart S, Driessche IV, Palau A, Puig T, Obradors X (2013) Flexible manufacturing of functional ceramic coatings by inkjet printing. Thin Solid Films 548:489–497
Villar G, Graham A, Bayley H (2013) A tissue-like printed material. Science 340(6128):48–52
Vos H, Dollet B, Versluis M, de Jong N (2011) Nonspherical shape oscillations of coated microbubbles in contact with a wall. Ultrasound Med Biol 37(6):935–948
Wijshoff H (2010) The dynamics of the piezo inkjet printhead operation. Phys Rep 491:77–177
Zhang J, Yan S, Yuan D, Alici G, Nguyen NT, Warkiani M, Li W (2016) Fundamentals and applications of inertial microfluidics: a review. Lab Chip 16(1):10–34

Affiliations

Arjan Fraters[1] · Tim Segers[1] · Marc van den Berg[2] · Hans Reinten[2] · Herman Wijshoff[2,3] · Detlef Lohse[1] · Michel Versluis[1]

Michel Versluis
m.versluis@utwente.nl

[1] Physics of Fluids Group, Max-Planck Center Twente for Complex Fluid Dynamics, Department of Science and Technology, MESA+ Institute, and J. M. Burgers Centre for Fluid Dynamics, University of Twente, P.O. Box 217, 7500 AE Enschede, The Netherlands

[2] Océ Technologies B.V., P.O. Box 101, 5900 MA Venlo, The Netherlands

[3] Department of Mechanical Engineering, Eindhoven University of Technology, P.O. Box 513, 5600 MB Eindhoven, The Netherlands